



Journal Name

ARTICLE

Isorecticular Zirconium-Based Metal-Organic Frameworks: Discovering Mechanical Trends and Elastic Anomalies Controlling Chemical Structure Stability

Matthew R. Ryder,^a Bartolomeo Civalleri,^b and Jin-Chong Tan^{a*}Received 00th January 20xx,
Accepted 00th January 20xx

DOI: 10.1039/x0xx00000x

www.rsc.org/

Understanding the mechanical properties of metal-organic frameworks (MOFs) is crucial not only to yield robust practical applications, but also to advance fundamental research underpinning the flexibility of a myriad of open-framework chemical compounds. Herein we present one of the most comprehensive structural analyses yet on MOF-mechanics: elucidating the complex elastic response of an isorecticular series of topical Zr-based MOFs, explaining all the important mechanical properties, and identifying major trends arising from systematic organic linker exchange. *Ab initio* density functional theory (DFT) was employed to establish the single-crystal elastic constants of the nanoporous MIL-140(A-D) structures, generating a complete 3-D representation of the principal mechanical properties, encompassing the Young's modulus, shear modulus, linear compressibility and Poisson's ratio. Of particular interest, we discovered significantly high values of both positive and negative linear compressibility and Poisson's ratio, whose framework molecular mechanisms responsible for such elastic anomalies have been fully revealed. In addition to pinpointing large elastic anisotropy and unusual physical properties, we analyzed the bulk modulus of isorecticular Zr-MOF compounds to understand the framework structural resistance against the hydrostatic pressure, and determined the averaged mechanical behaviour of bulk (polycrystalline) MOF materials important for design of emergent applications.

1. Introduction

Metal-organic frameworks (MOFs)¹ have generated considerable interest due to their vast physical and chemical versatility^{2, 3} which can yield wide-ranging technological applications. MOFs are hybrid materials constructed from metal ions and organic linkers self-assembled at the molecular level producing a cornucopia of porous crystalline frameworks united by strong bonds.^{4, 5} One of the most fascinating aspects of MOFs is their large surface area, typically in the range of 1,000 to 10,000 m² g⁻¹.^{4, 6} These materials can be tailored for a remarkable array of multifunctional applications, which includes not only gas separation and storage⁷ that are traditionally associated with porous materials, but also emergent technologies varying from proton conductivity,⁸ opto-electronics⁹ and dielectrics¹⁰ to drug delivery and bio-sensing.^{11, 12}

Some of the most fascinating families of MOFs are porous compounds whose physical structure and chemical affinity can be manipulated, whilst keeping the basic topology of the framework consistent. These families are termed isorecticular

MOFs¹³ and the MIL-140 series^{14, 15} investigated in this work represents a promising example of such a system. The unique ability to rationally design, construct, and tune isorecticular MOFs has further expanded their possible applications. However, an important aspect of being able to take full advantage of all the promising applications is to address the robustness of MOFs in real-world manufacturing environments.^{16, 17} To this end, we will require reliable information of the mechanical properties of MOF chemical structures¹⁸ and knowledge about their structural durability and resilience,^{19, 20} both of which are relatively poorly understood. Likewise, engineering of certain practical applications (e.g. mechano-chemical sensors)^{12, 21} need comprehensive and accurate mechanical properties data to design for optimal device performance and lifetime.²² Mechanical tunability²³ of MOFs as a result of chemical structural modifications and strong host-guest interactions is also attractive for novel applications.

The number of studies concerned with understanding the basic elastic behaviour of MOFs is still relatively limited.^{6, 18, 24} Initially research concentrated on the Young's modulus (E)^{25, 26} and the bulk modulus (K),^{27, 28, 29} as these properties are more straightforward to characterize experimentally. However, especially for anisotropic materials such as MOFs, a more complete understanding of open framework structural mechanics^{30, 31} can be obtained only by considering other mechanical behaviour described by the shear modulus (G) and Poisson's ratio (ν). More recently, Brillouin scattering

^a Multifunctional Materials & Composites (MMC) Laboratory, Department of Engineering Science, University of Oxford, Parks Road, Oxford OX1 3PJ, United Kingdom.

^b Department of Chemistry, NIS Interdepartmental Centre and INSTM Reference Centre, University of Turin, via Pietro Giuria 7, 10125 Torino, Italy.
Electronic Supplementary Information (ESI) available: [Additional theoretical details, comparison with experiment and literature and additional 3-D plots of mechanical property surfaces.]. See DOI: 10.1039/x0xx00000x

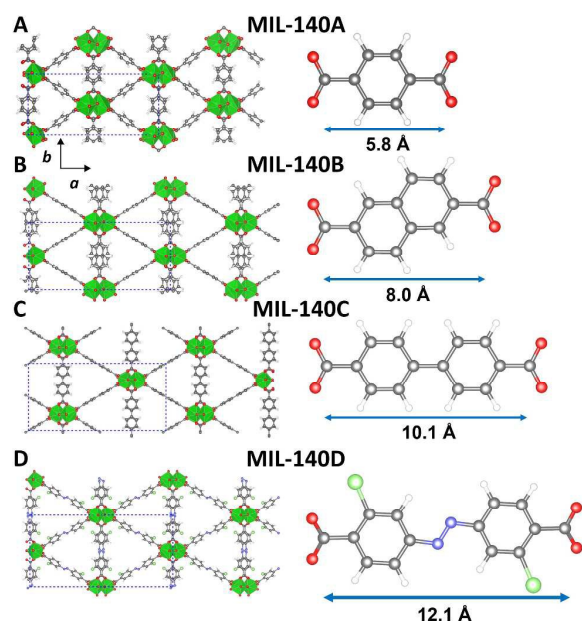


Fig. 1. (Left) Framework structures of the MIL-140 series featuring a general chemical formula $[\text{ZrO}(\text{O}_2\text{C-R-CO}_2)]$: (A) MIL-140A where $\text{R} = \text{C}_6\text{H}_4$, (B) MIL-140B ($\text{R} = \text{C}_{10}\text{H}_6$), (C) MIL-140C ($\text{R} = \text{C}_{12}\text{H}_8$) and (D) MIL-140D ($\text{R} = \text{C}_{12}\text{N}_2\text{H}_6\text{Cl}_2$).¹¹ The inorganic building units are ZrO_6 coordination polyhedra (green) forming 1-D chains along the crystal c -axis. The dashed blue lines represent one unit cell. (Right) Organic linkers of the respective frameworks. Color scheme adopted – zirconium: green; carbon: gray; oxygen: red; nitrogen: blue; chlorine: light green. The length of the linkers are defined as the distance from each carboxylate carbon.

experiments in conjunction with *ab initio* density functional theory (DFT) calculations were used to determine the complete elastic constants of cubic ZIF-8, from which a remarkably low shear modulus was found ($G \approx 1$ GPa).³² The low shear modulus suggested that there could be a heightened chance of shear-induced amorphisation from structural flexibility and framework destabilization,³³ which is supported by studies on the ball milling induced amorphisation of a large number of MOFs.^{34, 35} Notably the work on ZIF-8³² demonstrated that DFT is a powerful approach capable of establishing the full sets of elastic properties, which are extremely difficult to measure (particularly for low-symmetry crystals).³¹ There has since been a number of representative MOF structures^{36, 37} and related framework materials³⁸ that have been studied using the *ab initio* DFT approach. Although previous studies attempted to link the MOF mechanical properties to the geometry and compliance of the frameworks, they have yet to fully address the exact chemical

structure trends or explain precisely the mechanisms responsible for elastic anomalies associated with shear distortions and counterintuitive Poisson's ratio. These studies have, nonetheless, demonstrated that DFT can be used efficiently to analyse a wide selection of MOF materials with varying metals, linkers, porosity and network topologies.

In the current work, we study the detailed elastic properties and mechanical behaviour of the entire zirconium (Zr)-based MIL-140 series of isorecticular materials by means of DFT. The series consists of 4 unique materials obtained by varying the complexity of the dicarboxylic acid derived linkers, starting from with terephthalic acid, one of the simplest dicarboxylic acid after oxalic acid,³⁹ and the most simplest containing an aromatic ring. This particular series: MIL-140(A-D)^{14, 15} whose chemical structures are shown in Fig. 1, is ideal for understanding precisely how MOF mechanics is affected by the systematic expansion of a porous isorecticular framework. The MIL-140 structures are polymorphs of the topical UiO-66(Zr) material⁴⁰ but instead of isolated Zr_6O metal-oxo clusters, in the MIL-140 frameworks, infinite 1-D zirconium oxide (ZrO) chains act as secondary building units (SBU) and are located along the crystallographic c -axis (Fig. 1). Experiments have demonstrated that UiO-66(Zr) has excellent thermal and chemical stabilities,⁴⁰ albeit its mechanical stability against structural collapse (amorphisation) has recently been measured to be inferior to those of MIL-140.³⁵ Furthermore it has been suggested that,¹⁴ the enhanced hydrothermal stability of MIL-140 is a result of both the reduced flexibility of its 1-D ZrO chains (compared to Zr_6O clusters in UiO-66) together with the $\pi\cdots\pi$ interactions of the aromatic rings of the MIL-140 linkers. Although Zr-based MOFs are gaining major popularity in latest mainstream scientific literature,^{15, 41} relatively little in fact is reported about their underpinning mechanical trends.

2. Results and Discussion

2.1 First-Principles Quantum Mechanical Computations

We computed the theoretical single-crystal elastic constants (C_{ij} 's) of the four MIL-140(A-D) porous framework structures using first-principles density functional theory (DFT). We adopted the B3LYP hybrid exchange-correlation functional⁴², as recent studies have shown it to produce accurate results, and all-electron atom-centred Gaussian type basis sets, as implemented by the periodic *ab initio* CRYSTAL14 code.⁴³ This computational methodology has recently been validated on a prototypical MOF structure, whose elastic

TABLE 1 Single-crystal elastic stiffness constants (C_{ij} 's) of MIL-140(A-D). The monoclinic crystal symmetry entails 13 independent elastic coefficients.

Structure	C_{11}	C_{22}	C_{33}	C_{44}	C_{55}	C_{66}	C_{12}	C_{13}	C_{15}	C_{23}	C_{25}	C_{35}	C_{46}
MIL-140A	94.0	163.0	52.7	3.2	9.1	27.4	42.7	29.6	-4.0	17.4	0.3	-10.4	0.1
MIL-140B	80.5	143.1	47.2	5.0	6.6	20.9	36.4	29.3	11.7	12.3	4.6	2.1	6.4
MIL-140C	64.0	129.2	32.6	2.4	4.3	18.4	30.2	17.7	-10.5	12.6	-4.1	-2.7	-4.2
MIL-140D	62.2	109.4	29.3	1.6	3.0	17.0	25.2	17.6	7.2	8.4	2.8	0.1	3.6

TABLE 2 Elastic properties of MIL-140(A-D). Young's and shear moduli anisotropy are $A_E = E_{\max}/E_{\min}$ and $A_G = G_{\max}/G_{\min}$, respectively.

Elastic property		MIL-140 series			
		A	B	C	D
Young's modulus (GPa)	E_{\max}	142.0	126.5	114.0	99.2
	E_{\min}	11.3	9.6	4.8	3.0
	A_E	12.6	13.2	23.8	33.1
Shear modulus (GPa)	G_{\max}	36.9	32.7	29.2	26.8
	G_{\min}	3.2	2.7	1.3	0.8
	A_G	11.5	12.1	22.4	33.5
Linear compressibility (TPa^{-1})	β_{\max}	27.8	23.8	52.5	35.4
	β_{\min}	-3.0	0.2	-10.0	1.1
Poisson's ratio	ν_{\max}	1.11	0.98	1.16	1.37
	ν_{\min}	-0.13	-0.15	-0.29	-0.61
Ledbetter anisotropy	A^*	12.5	13.6	23.1	36.9

constants have been confirmed *via* Brillouin scattering experiments.³² A full relaxation of both lattice parameters and atomic coordinates was allowed to optimize the structures. Each elastic stiffness tensor was then computed by using the numerical first derivative of the analytic cell gradients, which corresponds to the individual elastic stiffness coefficients C_{ij} 's.⁴⁴ The coefficients were obtained as a result of deforming the optimized structure in the symmetrically required directions of both positive and negative strain amplitudes, thereby corresponding to the linear elastic stress-strain relationship. Further computational details are given in the Supporting Information (SI).

2.2 Tensorial Analysis to Construct the Full Picture of Elastic Anisotropy of Isorecticular Structures

Table 1 summarizes the calculated single-crystal elastic coefficients (C_{ij} 's). All four MIL-140(A-D) structures are monoclinic and hence have thirteen unique elastic constants. On the main diagonal of the elasticity tensor, the coefficients C_{11} , C_{22} and C_{33} represent the framework stiffness along the three principal crystallographic orientations (a -, b -, and c -axis respectively) under a uniaxial strain. The shear coefficients C_{44} , C_{55} and C_{66} signify the framework stiffness against an angular deformation when subjected to a shear strain. The remaining coefficients represent stiffness couplings. Specifically, the C_{12} , C_{13} and C_{23} coefficients are tensile–tensile coupling between two principal cell axes; the C_{15} , C_{25} and C_{35} coefficients represent the tensile–shear coupling, and the stiffness under shear–shear coupling is represented by the C_{46} coefficient. Directionally dependent mechanical properties were derived from these elastic coefficients by means of tensorial analysis using the Mathematica⁴⁵ and the EIAM codes.⁴⁶ The maximum and minimum values of various elastic properties, together with the extent of elastic anisotropy are summarized in

Table 2. The properties are namely: Young's modulus (E), shear modulus (G), linear compressibility (β), Poisson's ratio (ν) and Ledbetter anisotropy (A^*) and are defined in detail in the following sections.

2.3 Young's Modulus Describing Framework Stiffness Response in Uniaxial Stress State

We start by describing the Young's modulus (E), which is the ratio of uniaxial stress (σ) to uniaxial strain (ϵ) in one-dimensional elastic deformation. As such by definition, E is analogous to the stiffness property (i.e. ratio of load to displacement) of a classical Hookean spring. However, it can be seen in Fig. 2 that the framework stiffness response of the single crystals of MIL-140(A-D) are markedly anisotropic. The 3-D representation of the Young's modulus of MIL-140A is shown in Fig. 2A, where the surface corresponds to a spherical plot of $E(\mathbf{u})$ by varying the unit vector \mathbf{u} . Fig. 2B presents the systematic trends determined in the maximum and minimum Young's moduli for MIL-140(A-D), along with the corresponding degree of anisotropies ($A_E = E_{\max}/E_{\min}$). Interestingly, we found the general morphology and shape of the anisotropic E surfaces are similar for each structure (see SI Fig. S1). The extent of anisotropy increases when going

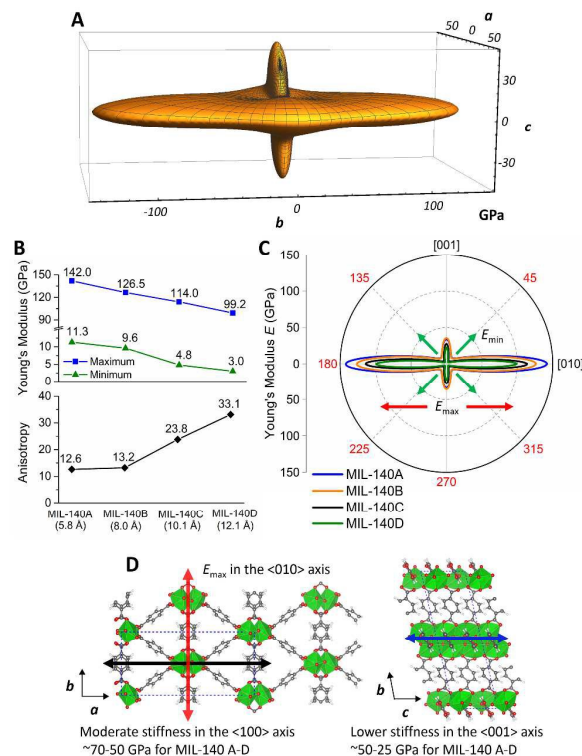


Fig. 2. (A) Young's modulus representation surface $E(\vartheta, \varphi)$ in 3-D spherical coordinates. MIL-140A where its E_{\max} is along the $\langle 010 \rangle$ axis. (B) Trends in the maximum and minimum stiffness (E_{\max} & E_{\min}) and their anisotropy values (A_E). (C) 2-D representation of the projections down the c -axis, showing E_{\min} in the vicinity of $\langle 011 \rangle$ crystal axis and the approximately self-similar stiffness profiles of $E_{\langle 001 \rangle}$. (D) Framework diagrams elucidating the origin of the directional Young's modulus along

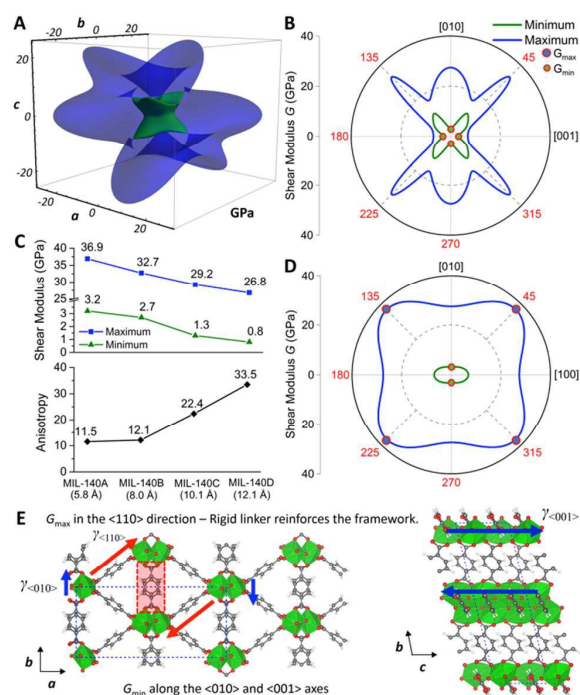


Fig. 3. (A) Shear modulus representation surface $G(\vartheta, \varphi, \chi)$ of MIL-140A in 3-D spherical coordinates, where the color coding: blue and green denotes the maximum and minimum moduli respectively. (B) trends in G_{\max} , G_{\min} and the anisotropy values (C) 2-D representation of the (100) plane; (D) 2-D representation of the (001) plane; (E) Diagram showing the origin of the maximum and minimum shear modulus for MIL-140A. Red dotted box highlights the position of the reinforcing linker.

through the reticular series, specifically the values of anisotropy (A_E) are 12.6, 13.2, 23.8 and 33.1 for MIL-140 from A to D, respectively. These magnitudes are also consistent with the Ledbetter anisotropy values (A^*), also shown in Table 2, which are established from the ratio of transverse sound velocities (V_{\min}^2/V_{\max}^2).⁴⁷ The elastic response along each axis can be explained by the underlying framework design, shown in Fig. 2D. The maximum for each framework, observed along the $\langle 010 \rangle$ crystal axis (values given in Fig. 2B), is the result of the rigid organic linkers (aligned in the b -axis) and the strain energy required to deform the aromatic rings. As would be expected, when additional structural flexibility (higher degrees of freedom) is introduced in the linker, the Young's modulus decreases. It is also worth noting that there will be an additional (linear) decrease expected in the Young's modulus going through the series, due to the presence of increased porosity. This is why we have evidenced an almost linear decline of uniaxial stiffness when stepping through the MIL-140 series, reflecting the nearly steady rise in linker length from structure A to D (Fig. 1). The second direction of interest is the $\langle 100 \rangle$ axis along which moderate stiffness have been determined, and this can be explained by the compression of the 3-noded ring architecture with each node constituting a Zr polyhedra. The third direction along the $\langle 001 \rangle$ axis is due to the 1-D chains of Zr polyhedra, conferring a relatively lower stiffness. We established that the variation in the Young's

moduli of the $\langle 100 \rangle$ and $\langle 001 \rangle$ axes going from MIL-140A to MIL-140D are less drastic (~ 70 -50 and ~ 50 -25 GPa respectively) than the variation of the maximum moduli (E_{\max}) along the $\langle 010 \rangle$ axis, as these crystallographic orientations are less strongly affected by the flexibility of the rigid linkers, supporting the claim that the ligand flexibility plays a significant role in addition to simply the increase in porosity.

2.3 Shear Modulus Defining Framework Rigidity Against Structural Distortion

Turning to the shear modulus (G), which is defined as the ratio of shear stress (τ) to shear strain (γ) under the influence of a pair of anti-parallel shearing forces. In essence, G characterizes the rigidity of the framework structure against an angular deformation or shape distortion. A 3-D representation surface of the shear modulus of MIL-140A is shown in Fig. 3A, whose 2-D projections normal to the (100) and (001) planes are given in Fig. 3B, D. It differs from that of the Young's modulus (Fig. 2), as the shear modulus, $G(\mathbf{u}, \mathbf{n})$ is a function of two unit vectors and hence is a 4-D property.⁴⁶ As presented in Fig. 3, we therefore limit the additional parameter (χ) to plot only maximum and minimum values of the 3-D shear modulus, shown in blue and green respectively. The monotonic trend in the maximum and minimum shear moduli for MIL-140(A-D), along with the corresponding anisotropies are mimicking that observed for the Young's modulus. Particularly, one should recognize that these trends are consistent with recent mechanical stability experiments conducted on the same series *via* ball milling,³⁵ in which the grinding time required to cause mechanical collapse (framework amorphisation) decreased in the same sequence in line with declining extremal shear moduli (Fig. 3C): MIL-140A > MIL-140B > MIL-140C > MIL-140D.

The general shape of the anisotropic shear modulus surfaces are again similar for each structure and can be seen in the SI (Fig. S2), endorsing the observed trends. The maximum shear modulus (G_{\max}) for all MIL-140 structures is located in the vicinity of the $\langle 110 \rangle$ directions (small deviations due to the angle of the linker). This can be explained by the rigid linker reinforcing the (otherwise pliant) 4-noded framework structure, this mechanism is illustrated in Fig. 3E. The reduction in the maximum shear modulus, as we go through the MIL-140 series, is associated with the reduction in the rigidity of the longer linker enhancing flexibility. The minimum shear modulus (G_{\min}) is less obvious, we discovered that there are two separate mechanisms that may result in approximately the same low values (Fig. 3E). These minimal rigidity values are located in the vicinity of the $\langle 010 \rangle$ and $\langle 001 \rangle$ axes (again small deviations due to the angle of the linker). The connection between the two similar values is the 1-D chains of Zr polyhedra, where the shear strain exerted along the b -axis (denoted as $\gamma_{\langle 010 \rangle}$) generates an angular deformation of the 4-noded ring configuration, however this time in the absence of any structural resistance by the reinforcing linker because it is positioned parallel to $\gamma_{\langle 010 \rangle}$. Another pliant angular distortion mechanism which we identified along the c -axis (i.e. $\gamma_{\langle 001 \rangle}$), involves shearing the

'tunnel-shaped' pore of the framework, for which the reinforcing linkers essentially fold in the $\langle 001 \rangle$ directions thus maintaining their planarity.

2.4 Linear Compressibility and Its Negative Response

Now we discuss linear compressibility (β), which is a measure of directional contraction under hydrostatic pressure.

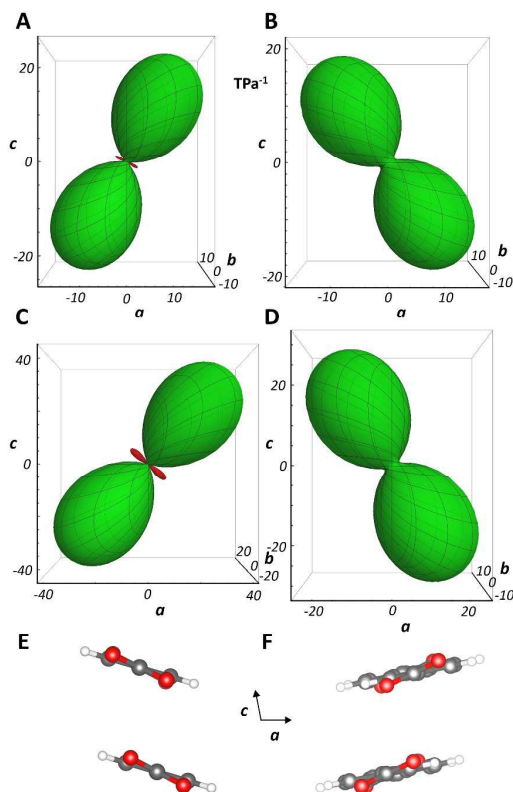


Fig. 4. Linear compressibility representation surface $\beta(\theta, \varphi)$ in 3-D spherical coordinates. (A) MIL-140A, (B) MIL-140B, (C) MIL-140C and (D) MIL-140D, where green and red designates positive and negative values of linear compressibility, respectively. Rings tilting in opposite directions for (E) MIL-140A versus (F) MIL-140B.

Fig. 4 shows the 3-D representation for each of the MIL-140 structures, where the surface corresponds to a spherical plot of $\beta(\mathbf{u})$ by varying the unit vector \mathbf{u} . The variation in the maximum and minimum linear compressibility for MIL-140(A-D) does not obey the same trend as the properties discussed above. While the general shape of the anisotropic surfaces are similar for each structure, interestingly the direction of the maximum and minimum is the same for MIL-140A and MIL-140C, but the opposite direction was determined for MIL-140B and MIL-140D. Another striking feature that these pairs have in common is that MIL-140A and MIL-140C both exhibit negative linear compressibility (NLC), whereas MIL-140B and MIL-140D do not. Indeed NLC is a rare and much sought after elastic anomaly,⁴⁸ whereby the framework experiences a linear expansion (instead of contraction) under hydrostatic pressure. We note that the NLC effects of both MIL-140A ($\beta_{\min} = -3 \text{ TPa}^{-1}$) and MIL-140C (-10 TPa^{-1}) are relatively strong, whose

magnitudes are on par with contemporary NLC materials, such as hybrid zinc formate (-1.8 TPa^{-1}),²⁸ $\text{Ag}_3[\text{Co}(\text{CN})_6]$ ($\approx -5 \text{ TPa}^{-1}$),⁴⁸ and a Ag-based MOF ($\approx -28 \text{ TPa}^{-1}$).⁴⁹

The maximum values of each framework can be understood by scrutinizing the π -stacking of the aromatic rings (Fig. 4E, F), with the stacking occurring approximately in the $\langle 001 \rangle$ axis and the rings tilting in the corresponding direction of the maximum for each structure. This explains why we see a reversal of the direction for MIL-140B and MIL-140D to that of MIL-140A and MIL-140C. Hence the direction of maximum linear compressibility (β_{\max}) is located in line with the direction of the centroid of the phenyl rings, since the attraction of the $\pi \cdots \pi$ stacking will allow for contraction upon hydrostatic compression. It follows that the minimum values (β_{\min}) will exist in the orthogonal direction to the maximum axis (due to phenyl ring rigidity), which matches the direction that is compressing the phenyl rings in plane. Furthermore, the NLC effect observed for MIL-140A and MIL-140C are likely to be the result of the phenyl rings rotating (yielding expansion) due to the higher level of rotational flexibility, when compared with the more rigid linker present in MIL-140B and the bulkier linker of MIL-140D. In particular, the presence of the bulky chlorine atoms of MIL-140D (see Fig. 1D) can lead to mechanical responses due to a balance between $\pi \cdots \pi$ stacking and repulsive force interactions. The negative values witnessed for MIL-140A and MIL-140C would encourage further experimental studies to investigate and further validate the postulated mechanisms suggested in this theoretical work.

2.5 Poisson's Ratio (ν) and Mechanism of Anomalous Auxeticity

Here we focus on the Poisson's ratio ($\nu_{ij} = -\epsilon_j/\epsilon_i$), which is defined as the quotient of lateral strain (ϵ_j) to axial strain (ϵ_i). Conventional isotropic materials typically feature a positive value of ν not exceeding 0.5,⁵⁰ since an axial expansion will be accompanied by a lateral contraction in transverse direction (and *vice versa*) such that volume is conserved. Being elastically anisotropic, however, the Poisson's ratio of the MIL-140s is complicated which can be seen as 3-D representations for MIL-140A and MIL-140D in Fig. 5A, B (also see SI Fig. S3). Because the Poisson's ratio is a function of two unit vectors $\nu(\mathbf{u}, \mathbf{n})$, we constrain the additional χ parameter to show only maximum and minimum values on the 3-D surfaces, shown in blue for the maximum and green and red for the positive and negative minima respectively.

The representation surface is highly anisotropic with the most interesting values being the 'auxetic' directions giving negative Poisson's ratios (NPR). The most auxetic direction, exhibiting $\nu_{\min} \approx -0.1$ to -0.6 (Table 2) is the result of a complex mechanism is not trivial to fully describe, but can be explained by the expansion of the 4-noded ring architecture (Fig. 5D) connected by ZrO_6 clusters behaving like hinges. This effect would be larger, if the structures were not 'reinforced' (by bridging ligand) and this has been demonstrated for example by Ortiz *et al.* for MIL-53.³⁶ Herein the NPR trend observed when going through the MIL-140 series (see Fig. 5C) is a systematic response to the reduction in the rigidity of the linker present. In addition, we established that the direction of

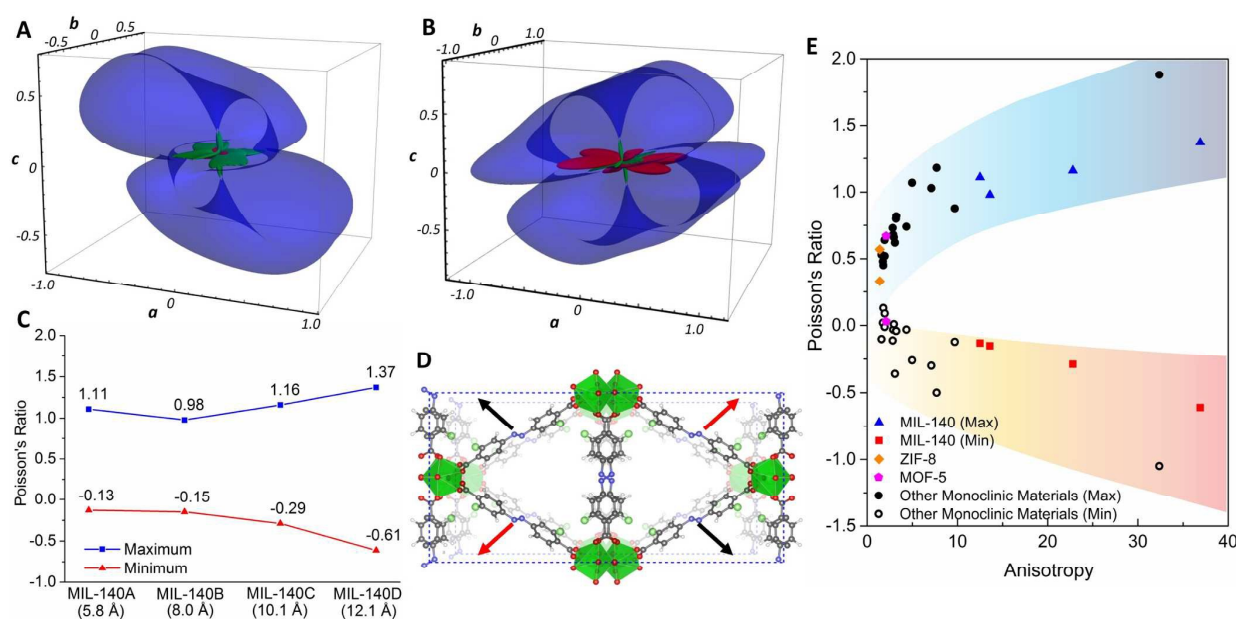


Fig. 5. Poisson's ratio representation surface $v(\theta, \phi, \chi)$ of (A) MIL-140A and (B) MIL-140D, where blue signifies the maximum Poisson's ratio and green and red denote the positive and negative minimum Poisson's ratios, respectively. (C) Trends in v_{\max} and v_{\min} . (D) Illustration of the auxetic mechanism responsible for the NPR response with the slightly transparent inset representing the original structure. (E) Correlation between the Ledbetter anisotropy A^* and extremal Poisson's ratios, incorporating data of other monoclinic materials,⁵¹ MOF-5³⁸ and ZIF-8.³² Blue and red bands designate the positive and negative Poisson's ratio respectively; the axial and transverse strain directions are summarized in SI Table S3.

the maximum Poisson's ratio is a result of the $\pi \cdots \pi$ interactions of the aromatic rings. This also explains the change in direction of the maximum Poisson's ratio witnessed for MIL-140A vs. MIL-140D due to the difference in the tilting of the aromatic rings (elaborated in former section on linear compressibility, see Fig. 4E, F). In Fig. 5E, it is promising to see that our values matched very well when comparing the relationship between both the maximum and minimum Poisson's ratio with the level of elastic anisotropy, to that of other monoclinic materials⁵¹ and also reported values for other MOF materials.

2.6 Bulk Modulus (K) and Polycrystalline Elastic Properties

Lastly moving away from the single-crystal properties, we will discuss the bulk modulus and present the averaged polycrystalline properties. These properties are of importance when considering MOFs in other forms than a single crystal. Good examples of this is the use of MOF materials in the form of pelletized powders,^{17, 52} randomly-oriented thin films and coatings^{3, 20} or compact polycrystalline membranes.⁵³ The bulk modulus for anisotropic materials is not an exact calculation and there are two main ways to obtain the value. The first is the Voigt method and the second is the Reuss method;⁵⁴ both methods are averaging techniques, where the Voigt assumes uniform strain and the Reuss assumes uniform stress. The most common way to report the bulk modulus for anisotropic materials is to give the average of the two and this is known as the Hill method. The resultant values are commonly called the Voigt-Reuss-Hill (VRH) averages,⁴⁶ which are given for MIL-140(A-D) in Table 3. The difference in the two main methods is

significant for example the Voigt and Reuss values for MIL-140A are 54.35 GPa and 36.21 GPa respectively. However, these values would indicate that the MIL-140 series are not particularly 'soft' under a hydrostatic pressure; by comparison we note the bulk moduli are appreciably lower for MOF-5 (~17 GPa),²⁵ ZIF-8 (~8 GPa)³² and even MIL-53-Al (~7 GPa).²⁹

It is also worth noting that all of the polycrystalline values for the Poisson's ratio are almost identical ($v_{\text{VRH}} \approx 0.35$ – 0.37) and clearly all positive. This result emphasizes the fact that in order to utilize the auxetic response discussed above (Fig. 5) for polycrystalline thin films, the materials would have to be grown for example in a controlled epitaxial manner to yield the desired crystal orientations.

3. Concluding Remarks

This work represents a comprehensive theoretical study to untangle the salient mechanical characteristics of an isoreticular series of Zr-based porous MOF material. Isoreticular MIL-140(A-D) compounds adopt the same network topology, though each structure features varying organic linker size and degree of flexibility. This provides the unique opportunity to precisely establish its primary structure-property trends, so as to explicate the fundamental connections that underpin elastic anisotropy and physical anomalies of MOFs. Significantly, the extremal shear moduli property trends we established here are in excellent

TABLE 3 Isotropic aggregate elastic properties based on the Voigt-Reuss-Hill (VRH) averages, corresponding to a texture-free polycrystalline material. The bulk (K), Young's (E) and shear (G) moduli are in GPa. Poisson's ratio (ν) is dimensionless.

Material	K_{VRH}	E_{VRH}	G_{VRH}	ν_{VRH}
MIL-140A	45.78	120.04	19.03	0.35
MIL-140B	41.36	35.64	13.14	0.36
MIL-140C	30.22	26.81	9.91	0.35
MIL-140D	28.74	22.99	8.41	0.37

correlation to recent experiments revealing the rates at which MIL-140 will undergo mechanically-induced amorphisation,³⁵ confirming the efficacy of applying rigorous elasticity theory to

promise of mechanical tunability for guiding rational design of isorecticular MOFs for specific applications.

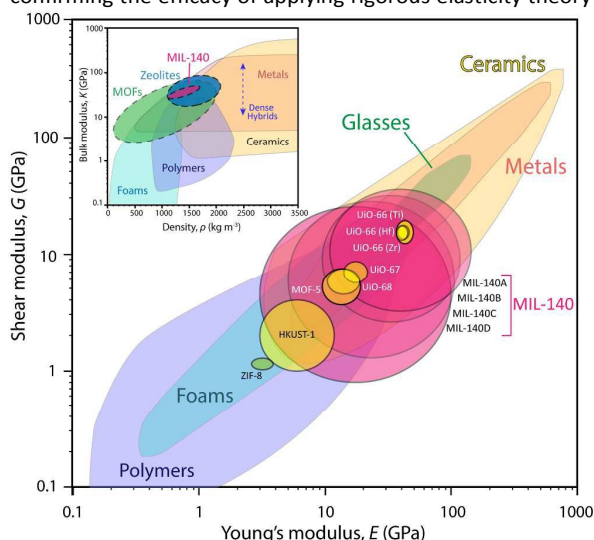


Fig. 6. Ashby-type materials selection chart showing the general relationship between shear modulus (G) and Young modulus (E). The inset shows the bulk modulus (K) property as a function of the physical density of different classes of technical materials. Noteworthy is the significant elastic anisotropy associated with the MIL-140(A-D) series, in comparison with the UiO counterparts and other topical MOFs (derived using DFT data from Ref. 18, 38).

explaining and forecasting structural stability trends of isorecticular MOF systems.

Our current work also lays the foundation to understanding the mechanical property landscape of isorecticular MOFs, as shown in Fig. 6, in relation to other major classes of 'conventional' technical materials for practical applications. The envelopes (Fig. 6) defining the shear and Young's moduli of MIL-140 are intersecting those of ceramics, metals, polymers and foams; thereby bridging the structural characters of the intrinsically 'rigid' inorganic solids and the relatively 'pliant' polymers; this effect is indeed significantly stronger than what was previously thought.¹⁸ The mechanical landscapes illustrated in Fig. 6 further emphasizes the enormous prospect to design, engineer, and fine tune the desired framework mechanics by exploiting isorecticular MOF chemistry. In fact, in isorecticular systems we discover that because the metal-coordination sites are identical, the structure-mechanical property trends can be rationalized on the basis of the length of the organic linkers. Finally, we show that *ab initio* computational models could offer valuable insights into the detailed physical mechanisms underpinning exotic MOF mechanics. Particularly, the source of counterintuitive phenomena such as negative linear compressibility (NLC) and negative Poisson's ratio (auxeticity) can be fully explained on the basis of the modular construction of MIL-140 frameworks. Our work sheds light on the general principles controlling chemical structure-to-mechanical behaviour correlations and demonstrates the significant

Acknowledgements

M.R.R. gratefully acknowledges postgraduate scholarships from the UK Engineering and Physical Sciences Research Council (EPSRC) DTA Award and the Science and Technology Facilities Council (STFC) Centre for Molecular Structure and Dynamics (CMSD) Award No. 13-05. We acknowledge the use of the University of Oxford Advanced Research Computing (ARC) facility in carrying out this work (<http://dx.doi.org/10.5281/zenodo.22558>). We thank the STFC e-Science Department for continued access to the SCARF cluster at the Rutherford Appleton Laboratory (RAL).

References

- H. C. Zhou, J. R. Long and O. M. Yaghi, *Chem Rev*, 2012, **112**, 673-674; G. Ferey and C. Serre, *Chem Soc Rev*, 2009, **38**, 1380-1399; C. N. R. Rao, A. K. Cheetham and A. Thirumurugan, *J. Phys.-Condens. Matter*, 2008, **20**, 083202; J.-C. Tan and B. Civalieri, *CrystEngComm*, 2015, **17**, 197-198.
- A. K. Chaudhari, I. Han and J. C. Tan, *Adv Mater*, 2015, DOI: 10.1002/adma.201501448, 4438-4446; N. Stock and S. Biswas, *Chem Rev*, 2012, **112**, 933-969; P. Falcaro, D. Buso, A. J. Hill and C. M. Doherty, *Adv Mater*, 2012, **24**, 3153-3168; M. S. Denny, Jr. and S. M. Cohen, *Angew Chem Int Ed Engl*, 2015, **54**, 9029-9032; B. Zornoza, C. Tellez, J. Coronas, J. Gascon and F. Kapteijn, *Micropor Mesopor Mat*, 2013, **166**, 67-78.
- O. Shekha, J. Liu, R. A. Fischer and C. Woll, *Chem Soc Rev*, 2011, **40**, 1081-1106.
- H. Furukawa, K. E. Cordova, M. O'Keeffe and O. M. Yaghi, *Science*, 2013, **341**, 1230444.
- O. K. Farha, I. Eryazici, N. C. Jeong, B. G. Hauser, C. E. Wilmer, A. A. Sarjeant, R. Q. Snurr, S. T. Nguyen, A. O. Yazaydin and J. T. Hupp, *Journal of the American Chemical Society*, 2012, **134**, 15016-15021.
- A. G. Slater and A. I. Cooper, *Science*, 2015, **348**, aaa8075.
- D. Peralta, G. Chaplais, A. Simon-Masseron, K. Barthelet, C. Chizallet, A. A. Quoineaud and G. D. Pirngruber, *Journal of the American Chemical Society*, 2012, **134**, 8115-8126; K. Sumida, D. L. Rogow, J. A. Mason, T. M. McDonald, E. D. Bloch, Z. R. Herm, T. H. Bae and J. R. Long, *Chem Rev*, 2012, **112**, 724-781; J. R. Li, J. Sculley and H. C. Zhou, *Chem Rev*, 2012, **112**, 869-932; T. Rodenas, I. Luz, G. Prieto, B. Seoane, H. Miro, A. Corma, F. Kapteijn, F. X. Llabres i Xamena and J. Gascon, *Nature materials*, 2015, **14**, 48-55.
- D. Umeyama, S. Horike, M. Inukai, T. Itakura and S. Kitagawa, *Journal of the American Chemical Society*, 2012, **134**, 12780-12785; P. Ramaswamy, N. E. Wong and G. K. Shimizu, *Chem Soc Rev*, 2014, **43**, 5913-5932.
- V. Stavila, A. A. Talin and M. D. Allendorf, *Chem Soc Rev*, 2014, **43**, 5994-6010; H. Khajavi, J. Gascon, J. M. Schins, L. D. A. Siebbeles and F. Kapteijn, *The Journal of Physical Chemistry C*, 2011, **115**, 12487-12493.
- K. Zagorodniy, G. Seifert and H. Hermann, *Applied Physics Letters*, 2010, **97**, 251905; S. Eslava, L. Zhang, S. Esconjauregui, J. Yang, K. Vanstreels, M. R. Baklanov and E. Saiz, *Chemistry of Materials*, 2013, **25**, 27-33.

11. A. C. McKinlay, J. F. Eubank, S. Wuttke, B. Xiao, P. S. Wheatley, P. Bazin, J. C. Lavalley, M. Daturi, A. Vimont, G. De Weireld, P. Horcajada, C. Serre and R. E. Morris, *Chemistry of Materials*, 2013, **25**, 1592-1599; J. Zhuang, C. H. Kuo, L. Y. Chou, D. Y. Liu, E. Weerapana and C. K. Tsung, *ACS Nano*, 2014, **8**, 2812-2819; P. Horcajada, R. Gref, T. Baati, P. K. Allan, G. Maurin, P. Couvreur, G. Ferey, R. E. Morris and C. Serre, *Chem Rev*, 2012, **112**, 1232-1268.
12. M. R. Ryder and J. C. Tan, *Materials Science and Technology*, 2014, **30**, 1598-1612.
13. O. M. Yaghi and Q. Li, *MRS Bull.*, 2011, **34**, 682-690; M. T. Wharmby, J. P. Mowat, S. P. Thompson and P. A. Wright, *Journal of the American Chemical Society*, 2011, **133**, 1266-1269; R. L. Martin, L.-C. Lin, K. Jariwala, B. Smit and M. Haranczyk, *The Journal of Physical Chemistry C*, 2013, **117**, 12159-12167; J. Gascon, M. D. Hernandez-Alonso, A. R. Almeida, G. P. van Klink, F. Kapteijn and G. Mul, *Chemsuschem*, 2008, **1**, 981-983.
14. V. Guillermin, F. Ragon, M. Dan-Hardi, T. Devic, M. Vishnuvarthan, B. Campo, A. Vimont, G. Clet, Q. Yang, G. Maurin, G. Ferey, A. Vittadini, S. Gross and C. Serre, *Angew Chem Int Ed Engl*, 2012, **51**, 9267-9271.
15. W. Liang, R. Babarao, T. L. Church and D. M. D'Alessandro, *Chem Commun (Camb)*, 2015, **51**, 11286-11289; B. Van de Voorde, D. Damasceno Borges, F. Vermoortele, R. Wouters, B. Bozbiyik, J. Denayer, F. Taulelle, C. Martineau, C. Serre, G. Maurin and D. De Vos, *Chemsuschem*, 2015, **8**, 3159-3166.
16. M. D. Allendorf and V. Stavila, *CrystEngComm*, 2015, **17**, 229-246.
17. D. Bazer-Bachi, L. Assié, V. Lecocq, B. Harbuzaru and V. Falk, *Powder Technology*, 2014, **255**, 52-59.
18. J. C. Tan and A. K. Cheetham, *Chem Soc Rev*, 2011, **40**, 1059-1080.
19. E. M. Mahdi and J.-C. Tan, *Journal of Membrane Science*, 2016, **498**, 276-290; N. W. Khun, E. M. Mahdi, S. Ying, T. Sui, A. M. Korsunsky and J.-C. Tan, *APL Mater*, 2014, **2**, 124101; I. Stassen, M. Styles, T. Van Assche, N. Campagnol, J. Franssaer, J. Denayer, J.-C. Tan, P. Falcaro, D. De Vos and R. Ameloot, *Chemistry of Materials*, 2015, **27**, 1801-1807.
20. I. Buchan, M. R. Ryder and J.-C. Tan, *Cryst Growth Des*, 2015, **15**, 1991-1999.
21. L. E. Kreno, K. Leong, O. K. Farha, M. Allendorf, R. P. Van Duyne and J. T. Hupp, *Chem Rev*, 2012, **112**, 1105-1125.
22. P. Silva, S. M. Vilela, J. P. Tome and F. A. Almeida Paz, *Chem Soc Rev*, 2015, **44**, 6774-6803; F. Mammeri, E. L. Bourhis, L. Rozes and C. Sanchez, *J Mater Chem*, 2005, **15**, 3787.
23. R. J. Marshall, S. L. Griffin, C. Wilson and R. S. Forgan, *Journal of the American Chemical Society*, 2015, **137**, 9527-9530; W. Li, A. Thirumurugan, P. T. Barton, Z. Lin, S. Henke, H. H. Yeung, M. T. Wharmby, E. G. Bithell, C. J. Howard and A. K. Cheetham, *Journal of the American Chemical Society*, 2014, **136**, 7801-7804.
24. W. Li, S. Henke and A. K. Cheetham, *APL Mater*, 2014, **2**, 123902.
25. D. F. Bahr, J. A. Reid, W. M. Mook, C. A. Bauer, R. Stumpf, A. J. Skulan, N. R. Moody, B. A. Simmons, M. M. Shindel and M. D. Allendorf, *Physical Review B*, 2007, **76**.
26. J. C. Tan, J. D. Furman and A. K. Cheetham, *Journal of the American Chemical Society*, 2009, **131**, 14252-14254; J. C. Tan, T. D. Bennett and A. K. Cheetham, *Proc Natl Acad Sci U S A*, 2010, **107**, 9938-9943; S. Henke, W. Li and A. K. Cheetham, *Chem Sci*, 2014, **5**, 2392.
27. K. W. Chapman, G. J. Halder and P. J. Chupas, *Journal of the American Chemical Society*, 2008, **130**, 10524-10526; T. D. Bennett, P. Simoncic, S. A. Moggach, F. Gozzo, P. Macchi, D. A. Keen, J. C. Tan and A. K. Cheetham, *Chem Commun (Camb)*, 2011, **47**, 7983-7985.
28. W. Li, M. R. Probert, M. Kosa, T. D. Bennett, A. Thirumurugan, R. P. Burwood, M. Parinello, J. A. Howard and A. K. Cheetham, *Journal of the American Chemical Society*, 2012, **134**, 11940-11943.
29. P. Serra-Crespo, A. Dikhtiarenko, E. Stavitski, J. Juan-Alcaniz, F. Kapteijn, F. X. Coudert and J. Gascon, *CrystEngComm*, 2015, **17**, 276-280.
30. M. de Jong, W. Chen, T. Angsten, A. Jain, R. Notestine, A. Gamst, M. Sluiter, C. Krishna Ande, S. van der Zwaag, J. J. Plata, C. Toher, S. Curtarolo, G. Ceder, K. A. Persson and M. Asta, *Sci Data*, 2015, **2**, 150009; J.-C. Tan, B. Civalieri, A. Erba and E. Albanese, *CrystEngComm*, 2015, **17**, 375-382; M. R. Ryder, B. Civalieri, G. Cinque and J.-C. Tan, *CrystEngComm*, 2016, DOI: 10.1039/c5ce02347e.
31. M. R. Ryder and J. C. Tan, *Dalton Transactions*, 2016, (In Press) DOI: 10.1039/C5DT03514G.
32. J. C. Tan, B. Civalieri, C. C. Lin, L. Valenzano, R. Galvelis, P. F. Chen, T. D. Bennett, C. Mellot-Draznieks, C. M. Zicovich-Wilson and A. K. Cheetham, *Phys Rev Lett*, 2012, **108**, 095502.
33. M. R. Ryder, B. Civalieri, T. D. Bennett, S. Henke, S. Rudic, G. Cinque, F. Fernandez-Alonso and J. C. Tan, *Phys Rev Lett*, 2014, **113**, 215502; J. Nishida, A. Tamimi, H. Fei, S. Pullen, S. Ott, S. M. Cohen and M. D. Fayer, *Proc Natl Acad Sci U S A*, 2014, **111**, 18442-18447.
34. T. D. Bennett and A. K. Cheetham, *Acc Chem Res*, 2014, **47**, 1555-1562; T. D. Bennett, S. Cao, J. C. Tan, D. A. Keen, E. G. Bithell, P. J. Beldon, T. Friscic and A. K. Cheetham, *Journal of the American Chemical Society*, 2011, **133**, 14546-14549.
35. B. Van de Voorde, I. Stassen, B. Bueken, F. Vermoortele, D. De Vos, R. Ameloot, J.-C. Tan and T. D. Bennett, *J. Mater. Chem. A*, 2015, **3**, 1737-1742.
36. A. U. Ortiz, A. Boutin, A. H. Fuchs and F. X. Coudert, *Phys Rev Lett*, 2012, **109**, 195502.
37. H. Wu, T. Yildirim and W. Zhou, *J Phys Chem Lett*, 2013, **4**, 925-930; F.-X. Coudert, A. Boutin, A. H. Fuchs and A. V. Neimark, *The Journal of Physical Chemistry Letters*, 2013, **4**, 3198-3205.
38. W. Zhou, H. Wu and T. Yildirim, *Chemical Physics Letters*, 2010, **499**, 103-107.
39. A. Buonaugurio, J. Graham, A. Buytendyk, K. H. Bowen, M. R. Ryder, Z. G. Keolopile, M. Haranczyk and M. Gutowski, *J Chem Phys*, 2014, **140**, 221103; Z. G. Keolopile, M. R. Ryder and M. Gutowski, *J Phys Chem A*, 2014, **118**, 7385-7391.
40. J. H. Cavka, S. Jakobsen, U. Olsbye, N. Guillou, C. Lamberti, S. Bordiga and K. P. Lillerud, *Journal of the American Chemical Society*, 2008, **130**, 13850-13851.
41. S. B. Kalidindi, S. Nayak, M. E. Briggs, S. Jansat, A. P. Katsoulidis, G. J. Miller, J. E. Warren, D. Antypov, F. Cora, B. Slater, M. R. Prestly, C. Marti-Gastaldo and M. J. Rosseinsky, *Angew Chem Int Ed Engl*, 2015, **54**, 221-226; J. E. Mondloch, M. J. Katz, W. C. Isley, 3rd, P. Ghosh, P. Liao, W. Bury, G. W. Wagner, M. G. Hall, J. B. DeCoste, G. W. Peterson, R. Q. Snurr, C. J. Cramer, J. T. Hupp and O. K. Farha, *Nature materials*, 2015, **14**, 512-516; P. Deria, D. A. Gomez-Gualdrón, W. Bury, H. T. Schaefer, T. C. Wang, P. K. Thallapally, A. A. Sarjeant, R. Q. Snurr, J. T. Hupp and O. K. Farha, *Journal of the American Chemical Society*, 2015, **137**, 13183-13190; Q. Zhang, J. Su, D. Feng, Z. Wei, X. Zou and H. C. Zhou, *Journal of the American Chemical Society*, 2015, **137**,

Journal Name

ARTICLE

- 10064-10067; X. Liu, N. K. Demir, Z. Wu and K. Li, *Journal of the American Chemical Society*, 2015, **137**, 6999-7002.
42. A. D. Becke, *The Journal of Chemical Physics*, 1993, **98**, 5648.
43. R. Dovesi, R. Orlando, A. Erba, C. M. Zicovich-Wilson, B. Civalieri, S. Casassa, L. Maschio, M. Ferrabone, M. De La Pierre, P. D'Arco, Y. Noël, M. Causà, M. Rérat and B. Kirtman, *International Journal of Quantum Chemistry*, 2014, **114**, 1287-1317.
44. W. F. Perger, J. Criswell, B. Civalieri and R. Dovesi, *Comput. Phys. Commun.*, 2009, **180**, 1753-1759.
45. Wolfram Research Inc., 2015.
46. A. Marmier, Z. A. D. Lethbridge, R. I. Walton, C. W. Smith, S. C. Parker and K. E. Evans, *Comput. Phys. Commun.*, 2010, **181**, 2102-2115.
47. H. Ledbetter and A. Migliori, *J Appl Phys*, 2006, **100**, 063516.
48. A. L. Goodwin, D. A. Keen and M. G. Tucker, *Proc Natl Acad Sci U S A*, 2008, **105**, 18708-18713.
49. W. Cai and A. Katrusiak, *Nat Commun*, 2014, **5**, 4337.
50. G. N. Greaves, A. L. Greer, R. S. Lakes and T. Rouxel, *Nature materials*, 2011, **10**, 823-837.
51. Z. A. D. Lethbridge, R. I. Walton, A. S. H. Marmier, C. W. Smith and K. E. Evans, *Acta Mater.*, 2010, **58**, 6444-6451.
52. G. W. Peterson, J. B. DeCoste, T. G. Glover, Y. Huang, H. Jasuja and K. S. Walton, *Micropor Mesopor Mat*, 2013, **179**, 48-53.
53. Y. S. Li, F. Y. Liang, H. Bux, A. Feldhoff, W. S. Yang and J. Caro, *Angew Chem Int Ed Engl*, 2010, **49**, 548-551; N. Rangnekar, N. Mittal, B. Elyassi, J. Caro and M. Tsapatsis, *Chem Soc Rev*, 2015, **44**, 7128-7154.
54. J. F. Nye, *Physical Properties of Crystals*, Clarendon Press, Oxford, 1985.